IPPP/13/103, DCPT/13/206, KCL-PH-TH/2013-48, DESY-13-258

Sharpening m_{T2} cusps: The mass determination of semi-invisibly decaying particles from a resonance.

Lucian A. Harland-Lang[1], Chun-Hay Kom[2], Kazuki Sakurai[3], and Marco Tonini[4]
[1] *Department of Physics and Institute for Particle Physics Phenomenology, University of Durham, DH1 3LE, UK*
[2] *Department of Mathematical Sciences, University of Liverpool Liverpool L69 3BX, UK*
[3] *Theoretical Particle Physics and Cosmology Group, Department of Physics, King's College London, London WC2R 2LS, UK and*
[4] *DESY Theory Group, Notkestr. 85, 22607 Hamburg, Germany*

We revisit mass determination techniques for the minimum symmetric event topology, namely X pair production followed by $X \to \ell N$, where X and N are unknown particles with the masses to be measured, and N is an invisible particle. We consider separate scenarios, with different initial constraints on the invisible particle momenta, and present a systematic method to identify the kinematically allowed mass regions in the (m_N, m_X) plane. These allowed regions exhibit a cusp structure at the true mass point, which is equivalent to the one observed in the m_{T2} endpoints in certain cases. By considering the boundary of the allowed mass region we systematically define kinematical variables which can be used in measuring the unknown masses, and find a new expression for the m_{T2} variable as well as its inverse. We explicitly apply our method to the case that X is pair produced from a resonance, and as a case study, we consider the process $pp \to A \to \tilde{\chi}_1^+ \tilde{\chi}_1^-$, followed by $\tilde{\chi}_1^\pm \to \ell\tilde{\nu}$, in the minimal supersymmetric standard model and show that our method provides a precise measurement of the chargino and sneutrino masses, m_X and m_N, at 14 TeV LHC with 300 fb^{-1} luminosity.

PACS numbers:

INTRODUCTION

The new physics search program at the Large Hadron Collider (LHC) is soon to enter its second phase. If new physics is observed at the LHC, the masses of the Beyond the Standard Model (BSM) particles will be one of the first observables to be measured. The strategy for measuring the masses of these particles is in general strongly dependent on the event topology but, interestingly, one particular case is predicted in a range of BSM models: the pair production of BSM particles, each of which subsequently decays, through cascade decay chains, to an invisible particle. So far, most studies have focused on relatively long (2 – 4 steps) 2–body cascade chains or a short 3–body decay chains, initiated by the production of coloured BSM particles [1–19][1]. However, the mass of coloured BSM particles is now strongly constrained by the null results of the BSM searches at the LHC. In the context of the Minimal Supersymmetric Standard Model (MSSM), the observation of a Higgs–like particle with $m_H \simeq 126$ GeV may also indicate that the gluino and squarks are heavier than the LHC reach [21, 22].

On the other hand, constraints on colour–singlet BSM particles are much weaker. However, as the decay chain is in this case typically a short, one–step process, namely X pair production followed by $X \to \ell N$ (see Fig. 1), where N is an invisible particle, measuring the two masses m_N and m_X is particularly challenging.

[1] See also [20] for a review.

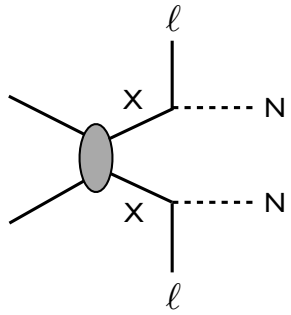

FIG. 1: One–step decay chain of a pair produced and semi–invisibly decaying particle X.

At a hadron collider, this event topology yields the "minimal" set of constraints

$$\Phi_{\text{min}} : \begin{cases} \tilde{m}_X^2 = (p_{\ell_1}^\mu + p_{N_1}^\mu)^2 = (p_{\ell_2}^\mu + p_{N_2}^\mu)^2 \\ \tilde{m}_N^2 = p_{N_1}^2 = p_{N_2}^2 \\ \not{p}^T = \mathbf{p}_{N_1}^T + \mathbf{p}_{N_2}^T \end{cases} \quad (1)$$

where $(\tilde{m}_N, \tilde{m}_X)$ need not coincide with the true mass values $\mathbf{m}^{\text{true}} \equiv (m_N, m_X)$, as they are a priori unknown. This set of constraints restricts the possible values of $\tilde{m}_N$ and $\tilde{m}_X$ and identifies a kinematically allowed region in the $(\tilde{m}_N, \tilde{m}_X)$ plane on an event–by–event basis. Furthermore, it is known [23] that the boundary of this allowed region under the Φ_{min} constraints coincides with

the m_{T2} variable [24]

$$\tilde{m}^{\rm min}_{X;\Phi_{\rm min}}(\tilde{m}_N) = m_{T2}(\tilde{m}_N) \equiv \min_{\sum_i \mathbf{p}^T_{N_i} = \not{p}^T} \left\{ \max \left[m_T(p^\mu_{\ell_1}, \mathbf{p}^T_{N_1}, \tilde{m}_N), m_T(p^\mu_{\ell_2}, \mathbf{p}^T_{N_2}, \tilde{m}_N) \right] \right\} \quad (2)$$

where m_T is the transverse mass [25]. In particular, the region with $\tilde{m}_X(\tilde{m}_N) < m_{T2}(\tilde{m}_N)$ is excluded in the zero width limit and for perfect detector resolution.

If the system is boosted in the transverse direction by e.g. hard initial state radiation (ISR), a collection of these $\tilde{m}_X(\tilde{m}_N)$ boundary curves from a large number of events exhibits a cusp structure [13, 14, 23, 26]. Fig. 2 shows the density of the boundary curves projected onto the $(\tilde{m}^2_X - \tilde{m}^2_N, \tilde{m}^2_N)$ plane, for the process $pp \to \tilde{q}\tilde{q}^*$, $\tilde{q} \to q\tilde{\chi}^+_1$, $\tilde{\chi}^+_1 \to \ell^+\tilde{\nu}_\ell$, with $(m_{\tilde{q}}, m_{\tilde{\chi}}, m_{\tilde{\nu}}) = (1500, 200, 100)$ GeV, and neglecting finite width effects and detector resolution. The combination of all the event–by–event kinematically allowed regions provides a "global" allowed region, corresponding to the right hand side white region in Fig. 2. Indeed, we find that the decay of the heavy squarks provides a "kick" to the di–X system, and a large boost in the transverse direction is achieved. Consequently, a cusp structure at the true mass point is observed. However, the population of the boundary curves around the cusp is very low and the cusp structure is not very distinct, even in this ideal case. In practice, the observation of this cusp is made even more difficult due to momentum mis–measurement and potential background contamination[2].

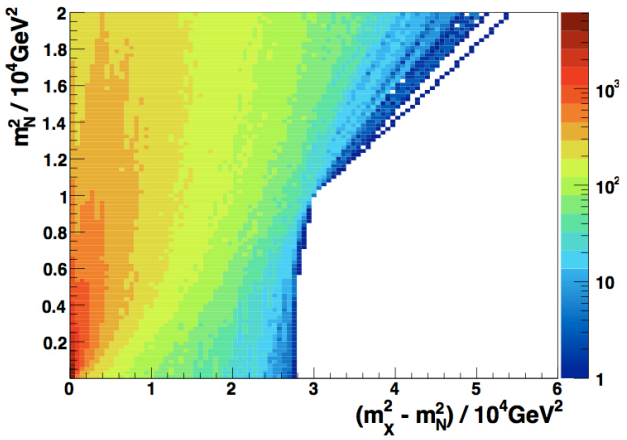

FIG. 2: Density plot of $\Phi_{\rm min}$ boundary curves for 10^4 $pp \to \tilde{q}\tilde{q}^* \to \tilde{\chi}^+_1\tilde{\chi}^-_1 q\bar{q} \to \left(e^+\tilde{\nu}_e\right)\left(e^-\tilde{\nu}^*_e\right) q\bar{q}$ LHC ($\sqrt{s} = 14$ TeV) events with $(m_{\tilde{q}}, m_{\tilde{\chi}}, m_{\tilde{\nu}}) = (1500, 200, 100)$ GeV, at the generator level.

[2] For studies along these lines, see [27, 28].

If one adds extra constraints to $\Phi_{\rm min}$, the kinematically allowed mass region is further restricted. Since the true mass point $\mathbf{m}^{\rm true}$ sits on the boundary of the global allowed region, adding such constraints will sharpen the cusp structure, and may make a simultaneous (m_N, m_X) measurement possible. A minimum and interesting possibility to extend $\Phi_{\rm min}$ is to add the constraint

$$\Phi_{\rm s}: \; m^2_A = (p^\mu_{\ell_1} + p^\mu_{N_1} + p^\mu_{\ell_2} + p^\mu_{N_2})^2 \; , \quad (3)$$

which is relevant to the case that the particle X is pair produced in the decay of a known resonance A (see Fig. 3).

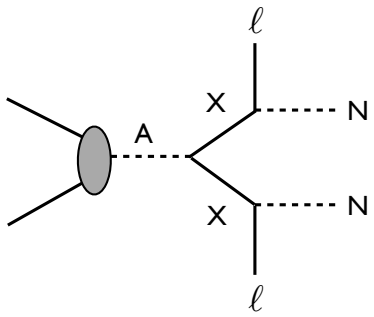

FIG. 3: Di–X production from a resonance A, followed by semi–invisible decays.

One of the goals of this paper is to develop a method to extract m_N and m_X from event samples with the topology shown in Fig. 3. As a benchmark scenario, we will investigate the LHC process $pp \to A \to \tilde{\chi}^+_1\tilde{\chi}^-_1 \to (l^+\tilde{\nu}_l)\,(l^-\tilde{\nu}^*_l)$, where A is the CP–odd Higgs boson of the MSSM, and demonstrate that one can measure $m_{\tilde{\chi}}$ and $m_{\tilde{\nu}}$ with good accuracy at 14 TeV LHC with 300 fb^{-1}.

In Fig. 4, we show a density plot for the boundary curves of the event–by–event allowed mass regions for this process. For concreteness, we take $(m_A, m_{\tilde{\chi}}, m_{\tilde{\nu}}) = (500, 200, 100)$ GeV. One can see that the kinematically allowed region, given by the lower white triangle (we note that the allowed region for each event lies below the corresponding boundary curve, and so the upper white region is excluded) is more restricted with respect to the $\Phi_{\rm min}$ case of Fig. 2 and that the cusp structure at the true mass point is more pronounced and more easily identified, reflecting the additional information which has been included, namely $\Phi_{\rm s}$.

Another way to extend $\Phi_{\rm min}$ is to assume that all four components of the missing momentum are known, namely by adding the constraint

$$\Phi_{\rm z}: \; \not{p}^z = p^z_{N_1} + p^z_{N_2} \; . \quad (4)$$

Notice that $\Phi_{\rm min} + \Phi_{\rm s} + \Phi_{\rm z} \equiv \Phi_{\rm max}$ is equivalent to $\Phi_{\rm min}$ with the last condition promoted to the Lorentz four–vector level $\not{p}^\mu = p^\mu_{N_1} + p^\mu_{N_2}$.

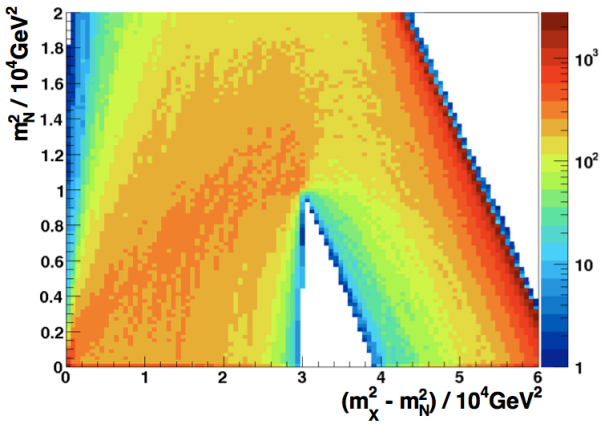

FIG. 4: Density plot of the $\Phi_{\rm min}+\Phi_{\rm s}$ boundary curves for 10^4 $pp\to A\to\tilde\chi_1^+\tilde\chi_1^-\to\left(l^+\tilde\nu_l\right)\left(l^-\tilde\nu_l^*\right)$ LHC ($\sqrt{s}=14$ TeV) events with $(m_A,m_{\tilde\chi},m_{\tilde\nu})=(500,200,100)$ GeV, at the generator level

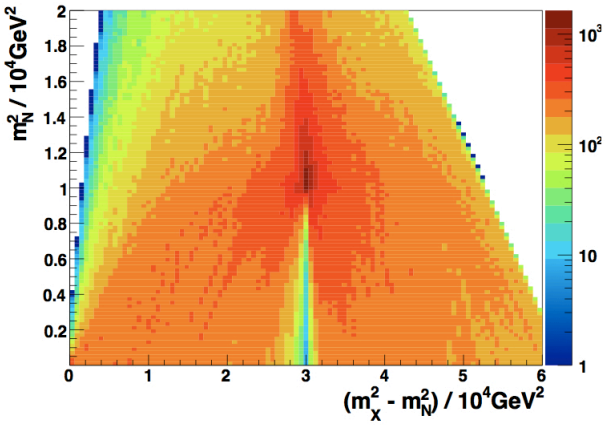

FIG. 5: Density plot of $\Phi_{\rm min}+\Phi_{\rm s}+\Phi_{\rm z}\equiv\Phi_{\rm max}$ boundary curves of 10^4 $e^+e^-\to\tilde e^+\tilde e^-\to\left(e^+\tilde\chi_1^0\right)\left(e^-\tilde\chi_1^0\right)$ ILC events with $(\sqrt{s},m_{\tilde e},m_{\tilde\chi})=(500,200,100)$ GeV, at the generator level.

This situation would be realised in a central exclusive process (CEP) with forward proton tagging at the LHC, $pp\to XX+pp$, $X\to\ell N$, or in the case of lepton colliders; a technique for extracting the masses (m_N,m_X) in these cases has been studied previously in [29, 30]. Notice that while at a lepton collider the invariant mass of the studied process is fixed by the center of mass energy of the collision, in the CEP case it is not a priori fixed but directly measured via proton tagging detectors. Assuming the set of constraints $\Phi_{\rm max}$, the global allowed region reduces to a straight line between the true mass point $(m_X^2-m_N^2,m_N)$ and $(m_X^2-m_N^2,0)$, as can be seen in Fig. 5, allowing for a precise simultaneous (m_N,m_X) measurement. In Fig. 5 we have shown equivalent density plots for a semi–invisible decay process at the ILC, namely $e^+e^-\to\tilde e^+\tilde e^-\to\left(e^+\tilde\chi_1^0\right)\left(e^-\tilde\chi_1^0\right)$ with $(\sqrt{s},m_{\tilde e},m_{\tilde\chi})=(500,200,100)$ GeV.

The paper is organized as follows. In the next section we will describe the kinematic variables used for the mass determination in our study. We will focus on their analytical form and their relation with other known kinematical variables such as m_{T2}. Furthermore we will clarify how their distribution for a large number of events could provide a simultaneous (m_N,m_X) mass measurement in a model–independent way. In the Results section we will then apply our method to the specific case of chargino and LSP mass measurement in events where two charginos are pair produced from the decay of the CP–odd Higgs A. Finally, we will summarize our results in the Conclusions.

MASS DETERMINATION METHOD

The use of the $\Phi_{\rm min}+\Phi_{\rm s}+\Phi_{\rm z}\equiv\Phi_{\rm max}$ constraints to develop a mass determination method [29, 30] serves as a starting point for our discussion on the implementation of the $\Phi_{\rm min}+\Phi_{\rm s}$ constraints. In particular, the purpose of the method described in [29, 30] was to determine all possible mass hypotheses $\tilde{\mathbf{m}}\equiv(\tilde m_N,\tilde m_X)$ consistent with the mass–shell constraints, and when all four components of $\not{p}^\mu$ are known. We will begin with a summary of the method applied in [29, 30], before considering the $\Phi_{\rm min}+\Phi_{\rm s}$ case.

In general, any $p^\mu_{N_1}$ and $p^\mu_{N_2}$ satisfying $\not{p}^\mu=p^\mu_{N_1}+p^\mu_{N_2}$ can be parametrised as

$$p^\mu_{N_1/N_2}=\frac{1\mp a}{2}\not{p}^\mu\pm\frac{b}{2}\,p^\mu_{\ell_1}\mp\frac{c}{2}\,p^\mu_{\ell_2}\pm d\,P^\mu\,,\qquad(5)$$

where a,b,c,d are dimensionless constants, and P^μ is a *space–like* vector defined by $P_\mu\equiv\epsilon_{\mu\nu\rho\sigma}\not{p}^\nu p^\rho_{\ell_1}p^\sigma_{\ell_2}$. Clearly we have $p^\mu_{X_1/X_2}=p^\mu_{N_1/N_2}+p^\mu_{\ell_1/\ell_2}$. With this parametrisation, the remaining $\Phi_{\rm max}$ constraints are given by

$$\tilde m_X^2=p_{X_1}^2=p_{X_2}^2,\qquad\tilde m_N^2=p_{N_1}^2=p_{N_2}^2,\qquad(6)$$

where again $\tilde{\mathbf{m}}$ are test mass values which need not coincide with the true masses $\mathbf{m}^{\rm true}$. For a given $\tilde{\mathbf{m}}$, the above four mass–shell conditions uniquely determine the coefficients a,b,c (see [30] for the explicit forms) and yield the equation

$$\lambda_N=\frac{c_a}{4\mathcal{M}}\lambda_\Delta^2+\frac{c_b}{2\mathcal{M}}\lambda_\Delta+\frac{c_c}{4\mathcal{M}}+d^2\lambda_P^2\,,\qquad(7)$$

where $\lambda_N\equiv\tilde m_N^2/(p_{\ell_1}\cdot p_{\ell_2})$, $\lambda_\Delta\equiv(\tilde m_X^2-\tilde m_N^2)/(p_{\ell_1}\cdot p_{\ell_2})$, and c_a,c_b,c_c and $\mathcal{M}$ are functions of p_{ℓ_1},p_{ℓ_2} and $\not{p}$ [30].

A hypothesis $\tilde{\mathbf{m}}$ is said to be consistent if the corresponding $\lambda_\Delta, \lambda_N$ lead to $d^2 > 0$, in order to obtain four–momenta p_i^μ with real components (5). In other words, in the $(\tilde{m}_N, \tilde{m}_X)$ plane, the region which leads to $d^2 > 0$ corresponds to kinematically consistent mass hypotheses, while the boundary of this region is identified from eq. (7) by setting $d = 0$. Furthermore, one can show that $c_a/4\mathcal{M} < 0$ [30], and thus the shape of the boundary is a parabola with negative curvature, containing the true mass point $\mathbf{m}^{\rm true}$ below its apex in the $(\tilde{m}_X^2 - \tilde{m}_N^2, \tilde{m}_N^2)$ plane.

As can be seen in Fig. 4 and Fig. 5, the sharp cusp structure observed in the $(\tilde{m}_X^2 - \tilde{m}_N^2, \tilde{m}_N^2)$ plane for the $\Phi_{\rm min}+\Phi_{\rm s}$ and $\Phi_{\rm max}$ cases would allow us to determine the true mass point by identifying the location of the cusps. Alternatively, one could define several *single* observables, whose distributions have endpoints at m_X or m_N. Such observables would be more useful in handling background contamination, detector effects, experimental uncertainties and so on. We first define the global maximum of $\tilde{m}_X$ and $\tilde{m}_N$ along the boundary, which can be expressed analytically as

$$
\begin{aligned}
(\tilde{m}^{\rm max}_{X;\Phi_{\rm max}})^2 &= \frac{p_{\ell_1}\cdot p_{\ell_2}}{4\mathcal{M}}\Big[c_c - \frac{(c_b+2\mathcal{M})^2}{c_a}\Big],\\
(\tilde{m}^{\rm max}_{N;\Phi_{\rm max}})^2 &= \frac{p_{\ell_1}\cdot p_{\ell_2}}{4\mathcal{M}}\Big[c_c - \frac{c_b^2}{c_a}\Big].
\end{aligned}
\tag{8}
$$

Other interesting variables which can be constructed are the extremal values of $\tilde{m}_X$ along the boundary, for a given hypothesis on $\tilde{m}_N$, denoted as $\tilde{m}^{\rm max/min}_{X;\Phi_{\rm max}}(\tilde{m}_N)$, and vice–versa $\tilde{m}^{\rm max/min}_{N;\Phi_{\rm max}}(\tilde{m}_X)$. Their analytical form is given by

$$
\begin{aligned}
\big[\tilde{m}^{\rm max/min}_{X;\Phi_{\rm max}}(\tilde{m}_N)\big]^2 &= \frac{p_{\ell_1}\cdot p_{\ell_2}}{c_a}\big[C_X \pm \sqrt{D_X}\big],\\
\big[\tilde{m}^{\rm max/min}_{N;\Phi_{\rm max}}(\tilde{m}_X)\big]^2 &= \frac{p_{\ell_1}\cdot p_{\ell_2}}{c_a}\big[C_N \pm \sqrt{D_N}\big]
\end{aligned}
\tag{9}
$$

where

$$
\begin{aligned}
C_N &= c_a\lambda_X + 2\mathcal{M} + c_b,\\
C_X &= c_a\lambda_N - c_b,\\
D_N &= (2\mathcal{M}+c_b)^2 + c_a(4\mathcal{M}\lambda_X - c_c),\\
D_X &= c_b^2 + c_a(4\mathcal{M}\lambda_N - c_c)
\end{aligned}
\tag{10}
$$

with $\lambda_X \equiv \tilde{m}_X^2/(p_{\ell_1}\cdot p_{\ell_2})$. Note that the $\pm$ in eq. (9) depends on the sign of $(p_{\ell_1}\cdot p_{\ell_2})/c_a$, i.e. in order to give a real solution for the max/min masses. The consistent mass region for a "typical" event, and the new kinematic variables which can be extracted are shown in Fig. 6.

By definition, the boundary variables defined above possess the following properties:

$$
\begin{aligned}
\tilde{m}^{\rm max}_{X;\Phi_{\rm max}} &\geq \tilde{m}^{\rm max}_{X;\Phi_{\rm max}}(m_N) \geq m_X,\\
\tilde{m}^{\rm min}_{X;\Phi_{\rm max}} &\leq \tilde{m}^{\rm min}_{X;\Phi_{\rm max}}(m_N) \leq m_X\ ,
\end{aligned}
\tag{11}
$$

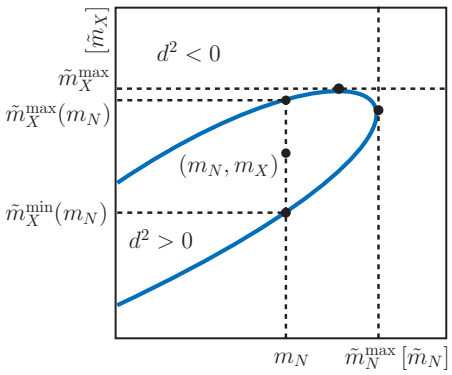

FIG. 6: Consistent $(\tilde{m}_N, \tilde{m}_X)$ region for a "typical" event, defined by the four–momenta $(p_{\ell_1}, p_{\ell_2}, \not{p})$. The $(d^2 > 0)$ consistent mass region contains by definition the true mass point (m_N, m_X). $\tilde{m}^{\rm max}_{N,X}$ are the maximum $\tilde{m}_N/\tilde{m}_X$ values, while $\tilde{m}_X^{\rm min,max}(m_N)$ is the minimal/maximal value of $\tilde{m}_X$ given m_N.

with similar relations for N. This observation has been used in [29, 30] to show that the distributions of $\tilde{m}^{\rm max}_{N;\Phi_{\rm max}}$ and $\tilde{m}^{\rm max}_{X;\Phi_{\rm max}}$ exhibit a sharp endpoint structure at the corresponding true masses in the case of CEP process and e^+e^- colliders, allowing for a precise simultaneous (m_N, m_X) measurement.

We will now consider the $\Phi_{\rm min}+\Phi_{\rm s}$ case. Here, the energy and longitudinal components of $\not{p}$ are unknown, reflecting the normal situation at the LHC, where a significant and unknown proportion of the energy of the incoming hadrons in each event escapes down the beam pipe, and therefore the longitudinal and energy components of the missing momentum are not determined. However, as the right hand side of eq. (9) is a function of these unknowns, $\not{p}^0$ and $\not{p}^z$, the boundary curve for the $\Phi_{\rm min}+\Phi_{\rm s}$ case and the corresponding kinematic variables can now be obtained by scanning over $\not{p}^0$ and $\not{p}^z$ under the constraint $\Phi_{\rm s}$, that is

$$
\begin{aligned}
\tilde{m}^{\rm max}_X(\tilde{m}_N) &= \max_{\{\not{p}^0,\not{p}^z\};\Phi_{\rm s}}\big[\tilde{m}^{\rm max}_{X;\Phi_{\rm max}}(\tilde{m}_N)\big],\\
\tilde{m}^{\rm min}_X(\tilde{m}_N) &= \min_{\{\not{p}^0,\not{p}^z\};\Phi_{\rm s}}\big[\tilde{m}^{\rm min}_{X;\Phi_{\rm max}}(\tilde{m}_N)\big],
\end{aligned}
\tag{12}
$$

with similar expressions for the N case. The global maximum variables can be obtained as

$$
\begin{aligned}
\tilde{m}^{\rm max}_X &= \max_{\{\not{p}^0,\not{p}^z\};\Phi_{\rm s}}\big[\tilde{m}^{\rm max}_{X;\Phi_{\rm max}}\big],\\
\tilde{m}^{\rm max}_N &= \max_{\{\not{p}^0,\not{p}^z\};\Phi_{\rm s}}\big[\tilde{m}^{\rm max}_{N;\Phi_{\rm max}}\big].
\end{aligned}
\tag{13}
$$

By definition, analogous relations as in eq. (11) are valid in this case

$$
\begin{aligned}
\tilde{m}^{\rm max}_{X/N} &\geq \tilde{m}^{\rm max}_{X/N}(m_{N/X}) \geq m_{X/N},\\
\tilde{m}^{\rm min}_{X/N} &\leq \tilde{m}^{\rm min}_{X/N}(m_{N/X}) \leq m_{X/N}.
\end{aligned}
\tag{14}
$$

We will see in the following section that the kinematic variables $\tilde{m}_N^{\max}$ and $\tilde{m}_X^{\min}(\tilde{m}_N)$ in fact possess the best discriminant power for a simultaneous (m_N, m_X) measurement in the $\Phi_{\min} + \Phi_{\rm s}$ case.

We now consider the relation of our kinematic variables to the m_{T2} variable. In analogy with the $\Phi_{\min}$ case (2), the kinematically allowed region under the $\Phi_{\min} + \Phi_{\rm s}$ constraints is in general bounded by m_{T2}

$$\tilde{m}_X^{\min}(\tilde{m}_N) \geq m_{T2}(\tilde{m}_N)\,, \tag{15}$$

where the inequality reflects the fact that additional information is provided by the $\Phi_{\rm s}$ constraint, further restricting $\tilde{m}_X(\tilde{m}_N)$. At the true invisible mass m_N the endpoint of the $m_{T2}(\tilde{m}_N = m_N)$ distribution coincides with the true mass m_X [13, 14]. Therefore, to draw a comparison and a cross–check of our method, for each event we have also evaluated the variable $m_{T2}(\tilde{m}_N)$, and studied its distribution for a large number of events.

Finally, we briefly return to the $\Phi_{\min}$ case. The boundary of the allowed mass region can be obtained in the same way as discussed above for the $\Phi_{\min} + \Phi_{\rm s}$ case, namely by scanning over $\not{p}^0$ and $\not{p}^z$ and taking the maximum or minimum depending on the variables. In Fig. 2, one can see that the allowed region is opened to $\tilde{m}_X \to \infty$, that is the variables $\tilde{m}^{\max}_{X;\Phi_{\min}}(\tilde{m}_N)$ and $\tilde{m}^{\min}_{N;\Phi_{\min}}(\tilde{m}_X)$ are not defined. Knowing that the boundary curve in the $\Phi_{\min}$ case is given by $m_{T2}(\tilde{m}_N)$ (2), we arrive at a new expression of the m_{T2} variable

$$m_{T2}(\tilde{m}_N) = \min_{\{\not{p}^0, \not{p}^z\}} \left[m^{\min}_{X;\Phi_{\max}}(\tilde{m}_N) \right]. \tag{16}$$

In the same way, an expression for the inverse m_{T2} function can be written down

$$m_{T2}^{-1}(\tilde{m}_X) = \max_{\{\not{p}^0, \not{p}^z\}} \left[m^{\max}_{N;\Phi_{\max}}(\tilde{m}_X) \right]. \tag{17}$$

This function has the following properties

$$m_{T2}^{-1}(m_X) \;\geq\; m_N, \tag{18}$$

$$m_{T2}^{-1}(m_{T2}(\tilde{m}_N)) \;=\; \tilde{m}_N. \tag{19}$$

RESULTS

To illustrate the features of our method we will consider the case of associated production of the MSSM CP–odd Higgs A with two b–jets, with the Higgs subsequently decaying into two charginos. We will then consider the decay of each chargino into a SM lepton plus a same flavour sneutrino, taken as the lightest supersymmetric particle in the spectrum. A final state with two opposite sign leptons, missing transverse energy and two b–jets will be therefore the topology under investigation.

It is worth stressing that the method we have presented here is independent of the particular underlying model.

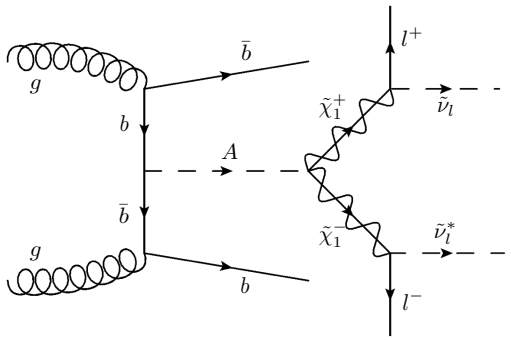

FIG. 7: Feynman diagram for the $pp \to Ab\bar{b} \to \chi_1^+\chi_1^-\, b\bar{b} \to \left(l^+\tilde{\nu}_l\right)\left(l^-\tilde{\nu}_l^*\right) b\bar{b}$ process considered in our study.

However, for concreteness, we have chosen a particular MSSM parameter space point. In particular we have taken $m_A = 800\,\text{GeV}$, $m_{\chi^\pm} = 350\,\text{GeV}$, $m_{\chi^0} = 300\,\text{GeV}$ and $m_{\tilde{\nu}} = 200\,\text{GeV}$. We have chosen as reference values $\tan\beta = 50$ and $\mu = 400\,\text{GeV}$, the former to increase the production cross section of the CP–odd Higgs for a given mass, the latter to increase the branching ratio into two charginos. Note that the dominant decay mode of the CP–odd Higgs is still into two bottom quarks, but we will assume that its mass m_A has already been measured with 10% precision from a dedicated study of the $A \to \tau^+\tau^-$ channel, similar to [31]. We will however conclude this paper by showing how our method could also be used to obtain a quite precise determination of the CP–odd Higgs mass, without such input.

The dominant backgrounds for the considered final state consist of direct chargino pair production plus jets, and SM $t\bar{t}$ and WW+jets processes with the W bosons decaying leptonically. A set of kinematic cuts has been chosen in order to maximize the signal over background ratio. In particular, each event is required to have exactly two opposite sign, same flavour leptons with $|\eta| < 2.5$, and two b–jets with $p_T > 20\,\text{GeV}$, $|\eta| < 2.5$. Moreover large cuts on the total missing transverse momentum ($\not{E}_T > 130\,\text{GeV}$), the p_T of the two leptons ($p_T^{l_1} > 80\,\text{GeV}$, $p_T^{l_2} > 40\,\text{GeV}$), and on the m_{T2} variable ($m_{T2} > 120\,\text{GeV}$) are applied to successfully reduce the backgrounds.

The associated CP–odd Higgs cross section has been calculated using FeynHiggs2.9.5 [32], the $\chi^+\chi^-$+jets using Prospino2.1 [33], while the values of the SM cross sections are reported in [34, 35]. The corresponding values are summarized in Table I. The branching ratio of the chargino into a lepton and same flavour sneutrino is set to 1.0, since the two–body decay into a W boson and a neutralino is kinematically forbidden for our parameter space choice. The leptonic branching ratio of the W boson is set to 0.216 [36]. MadGraph5 [37] is used to generate parton–level events, which are then interfaced with the Pythia 6.42 [38] parton shower. These are then

passed to Delphes 3.0 [39] to simulate the ATLAS detector in a fast manner, following the specifications reported in [31]. The public code described in [23] is used to evaluate m_{T2} for each event.

	$Ab\bar{b}$	$\chi^+\chi^-$+js	$t\bar{t}$	WW+js
$\sigma \cdot \mathrm{BR}$ [pb]	0.023	0.056	40.92	5.80

TABLE I: Cross sections at LHC14 for the signal and background processes considered in our study, before cuts.

A signal over background ratio of $S/B \sim 6.5$ with roughly 1000 remaining signal events is obtained with this setup, and the events passing the selection cuts are then used as input for our mass measurement method. In particular, we have simulated 100 independent signal and background measurements at LHC14 with 300 fb^{-1} integrated luminosity, to evaluate a statistical uncertainty on our observables.

In the following we attempt to measure m_N by measuring the endpoint of the $\tilde{m}_N^{\max}$ distribution: $m_N^{\exp} \equiv (\tilde{m}_N^{\max})^{\mathrm{endpoint}}$. We determine then m_X by measuring the endpoint of the $\tilde{m}_X^{\min}(m_N^{\exp})$ distribution: $m_X^{\exp} \equiv [\tilde{m}_X^{\min}(m_N^{\exp})]^{\mathrm{endpoint}}$.

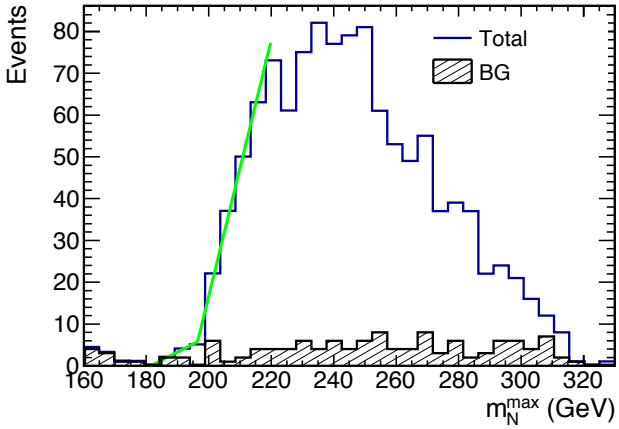

FIG. 8: $\tilde{m}_N^{\max}$ distribution of a single signal and background measurement at LHC14. The green line represents the fit used to determine the endpoint of the distribution.

In Fig. 8 we show a typical $\tilde{m}_N^{\max}$ distribution of a single LHC14 measurement. We fit the distribution by the two straight lines described by the function

$$f(x; x_0, a, b, c) = \Theta(x - x_0) \cdot a \cdot (x - x_0) + \\ + \Theta(x_0 - x) \cdot b \cdot (x_0 - x) + c\,, \qquad (20)$$

where x is the kinematical variable used in the x-axis, x_0 is the endpoint of the distribution, a and b are slopes of the two straight lines, and c is a constant term. From the fit we obtain a measurement of the invisible mass $m_N^{\exp}$ of

$$m_N^{\exp} = 194.5 \pm 1.9\,\mathrm{GeV}\,, \qquad (21)$$

remarkably close to the true value $m_N = 200\,\mathrm{GeV}$. All uncertainties are Gaussian statistical uncertainties coming from the 100 independent measurements.

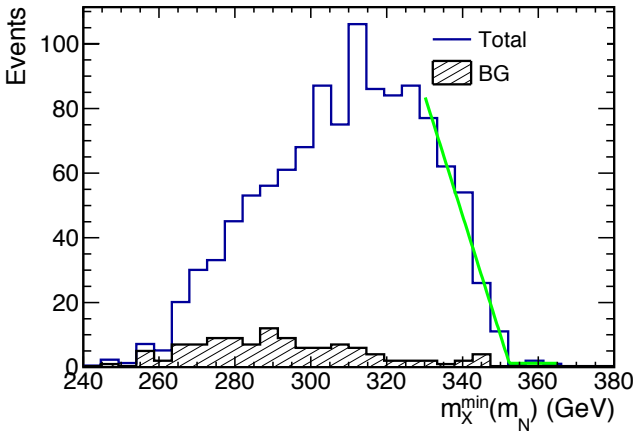

FIG. 9: $\tilde{m}_X^{\min}(m_N^{\exp})$ distribution of a single signal and background measurement at LHC14. The $m_N^{\exp}$ value has been extracted from the endpoint of the $\tilde{m}_N^{\max}$ distribution. The green line represents the fit used to determine the endpoint of the distribution.

In Fig. 9 we show a typical $\tilde{m}_X^{\min}(\tilde{m}_N)$ distribution of a single LHC14 measurement, where $\tilde{m}_N = m_N^{\exp} = 195.4\,\mathrm{GeV}$ is assumed. We obtain a measurement of the chargino mass $m_X^{\exp}$ of

$$m_X^{\exp} = 350.4 \pm 1.4\,\mathrm{GeV}\,, \qquad (22)$$

again remarkably close to the true value $m_X = 350\,\mathrm{GeV}$.

We have so far assumed that the mass of the resonance is precisely known. In realistic situations, our knowledge of m_A is limited by the experimental uncertainty. To study this effect, we interpret the m_A in eq. (3) as a variable and allow the observables defined in eqs. (12) and (13) to have dependency on $\tilde{m}_A$: $\tilde{m}_X^{\min}(\tilde{m}_A, \tilde{m}_N)$, $\tilde{m}_N^{\max}(\tilde{m}_A)$. In Fig. 10 we plot the endpoints of the $\tilde{m}_N^{\max}(\tilde{m}_A)$ distribution for different hypotheses on $\tilde{m}_A$. It is also shown how a 10% uncertainty on m_A affects this $m_N^{\exp}$ measurement, namely introducing a $\sim 20\%$ uncertainty.

The endpoints of the $\tilde{m}_X^{\min}(\tilde{m}_A, m_N^{\exp})$ distribution are shown in Fig. 11: for each $\tilde{m}_A$ hypothesis, we have determined the corresponding $m_N^{\exp}$ value, and then used this as an input for the $\tilde{m}_X^{\max}(\tilde{m}_A, m_N^{\exp})$ distribution. It is also shown how a 10% uncertainty on m_A affects the $m_X^{\exp}$ measurement, namely introducing a $\sim 20\%$ uncertainty.

It has previously been claimed that a simultaneous measurement of (m_N, m_X) is possible by using the kink structure arising in the distribution of the endpoints of the $m_{T2}(\tilde{m}_N)$ variable as a function of $\tilde{m}_N$, see [13, 14, 23]. However, this kink resides at the tail of

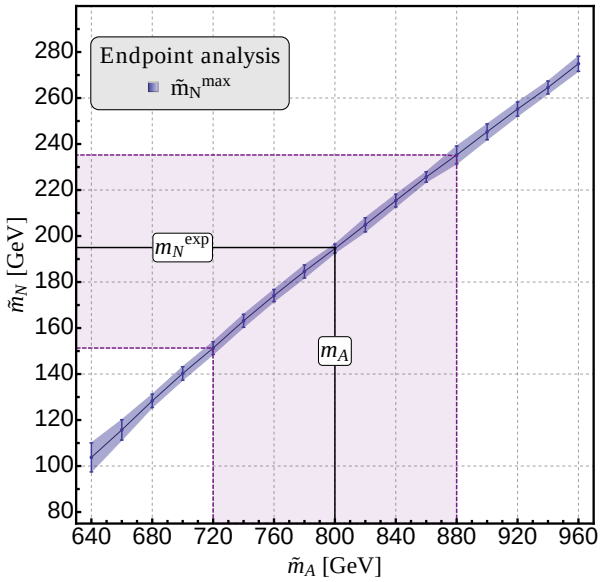

FIG. 10: Endpoint measurements of the $\tilde{m}_N^{\max}(\tilde{m}_A)$ distribution for different $\tilde{m}_A$ hypotheses. Each value represents the mean of 100 independent simulated measurements at LHC14. A band showing the effect of a 10% uncertainty on m_A is also shown.

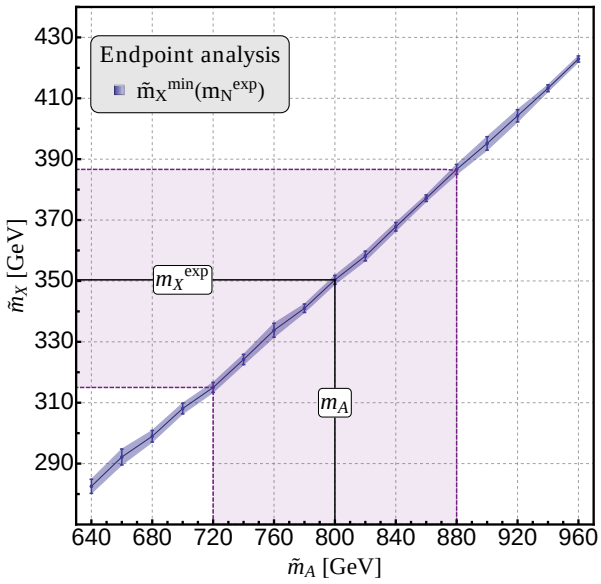

FIG. 11: Endpoint measurements of the $\tilde{m}_X^{\min}(\tilde{m}_A, m_N^{\exp})$ distribution for different $\tilde{m}_A$ hypotheses. Each value represents the mean of 100 independent simulated measurements at LHC14. A band showing the effect of a 10% uncertainty on m_A is also shown.

the $m_{T2}(\tilde{m}_N)$ distribution, making an accurate measurement difficult. However, even if such a kink structure is not evident, at the true invisible mass m_N the endpoint of the $m_{T2}(\tilde{m}_N = m_N)$ distribution for a large number of events should always coincide with the *mother* particle mass m_X, namely the chargino mass in our example. Therefore, by comparing the endpoints of the $\tilde{m}_X^{\min}(\tilde{m}_N)$ and $m_{T2}(\tilde{m}_N)$ distributions (assuming the true CP–odd Higgs mass m_A), we should be able to see that the two distributions coincide at $\mathbf{m}^{\text{true}}$, as can be clearly seen from Fig. 12.

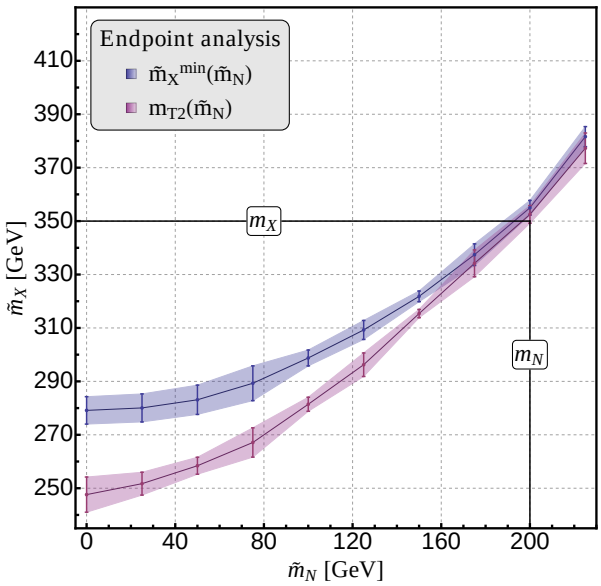

FIG. 12: $\tilde{m}_X^{\min}(\tilde{m}_N)$ and $m_{T2}(\tilde{m}_N)$ distributions as functions of $\tilde{m}_N$: they cross each other in the vicinity of the true masses $\mathbf{m}^{\text{true}}$.

The latter result should be viewed as a cross–check of the validity of our procedure rather than a direct measurement of the true masses, because of the rather large semi–overlapping region of the two curves. We can also see that there is not a clear kink structure in the $m_{T2}(\tilde{m}_N)$ distribution, and thus this could not provide a precise mass measurement, at least for the case we have considered.

Throughout the previous sections, the mass of the resonance, m_A, has been assumed to be already (well) measured, to within 10% uncertainty, in order to simultaneously evaluate $(m_N^{\exp}, m_X^{\exp})$. However, if a wrong value for m_A is used, then the Φ_{s} constraint of (3) no longer corresponds to the correct event kinematics, and one cannot expect the boundary variables, e.g. $\tilde{m}_N^{\max}$, to have a sharp endpoint structure. This observation may be used to measure the mass of the resonance.

For example, one can expect the slope of $\tilde{m}_N^{\max}(\tilde{m}_A)$ at the endpoint to become steeper as the input value, $\tilde{m}_A$, approaches m_A, where we will expect a sharper endpoint structure. This feature is indeed seen in Fig. 13, where we plot the slope of $\tilde{m}_N^{\max}$ at the vicinity of the endpoint as a function of $\tilde{m}_A$. This is obtained from the second straight line used in the endpoint fit (see the green line in Fig. 8),

which gives an estimate of the slope of this distribution as it approaches the endpoint. This behaviour is reasonably insensitive to precise parameters of the straight line fit and choice of bin size, and we expect it to hold for other mass choices. A more systematic understanding of this effect and its application to these and other mass measurements is the subject of ongoing studies.

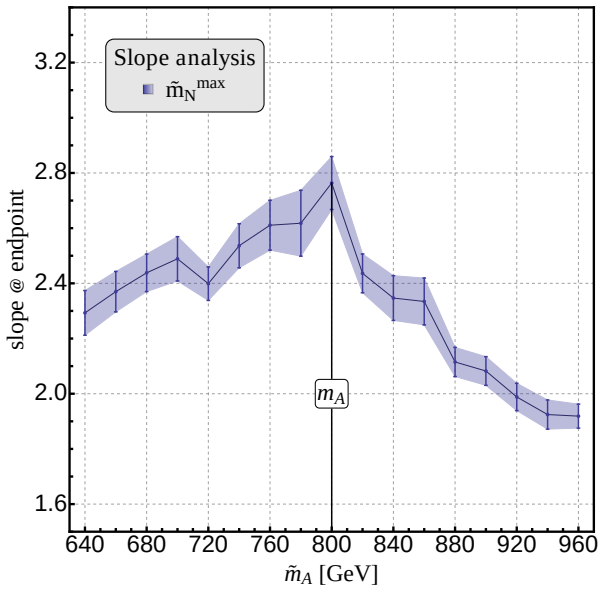

FIG. 13: Slope measurement at the endpoint of the $\tilde{m}_N^{\max}(\tilde{m}_A)$ distribution: the maximum is observed at $\tilde{m}_A = m_A$.

CONCLUSIONS

In this work a model–independent method for mass measurements at hadron colliders, in semi–invisible decay chains of pair produced particles, has been discussed. We have considered as a benchmark the process $p\,p \to A b\bar{b} \to \chi_1^+\chi_1^-\, b\bar{b} \to (l^+\tilde{\nu}_l)\,(l^-\tilde{\nu}_l^*)\, b\bar{b}$, where A is the MSSM CP–odd Higgs. Here, the chargino $\chi_1^\pm \equiv X$ and LSP $\tilde{\nu}_l \equiv N$ masses are undetermined. Analytic solutions of the final state system, taking into account the mass–shell conditions, constrain the possible $(\tilde{m}_N, \tilde{m}_X)$ mass hypotheses consistent with the measured momenta for each event. Given this kinematically consistent mass region, one can then construct new useful variables, and the distribution of these from a large number of events is found to exhibit a sharp endpoint at the true chargino and LSP masses, respectively.

In particular we have shown that with this method one can obtain a precise measurement of (m_N, m_X) at the $\sqrt{s} = 14\,\text{TeV}$ LHC, with $300\,\text{fb}^{-1}$ of integrated luminosity. It is to be noted that the only additional information that has to be provided is the mass of the resonance A, from whose decay the charginos are pair produced. The total missing momentum is not required to be an input of our analysis, as was considered in [29, 30]: our approach reflects a more realistic measurement scenario at the LHC.

Furthermore we have shown for our benchmark example that the value of the slope of the $\tilde{m}_N^{\max}$ distribution at the corresponding endpoint for different $\tilde{m}_A$ hypotheses develops a peak at the true mass m_A, and thus this fact could provide a guide to infer the mass of the resonance A. A more systematic understanding and application of this effect to mass measurements is the subject of ongoing studies.

Acknowledgements.— We thank Jürgen Reuter and Maikel de Vries for useful discussions. M.T. has been partially supported by the Deutsche Forschungsgemeinschaft within the Collaborative Research Center SFB 676 "Particles, Strings, Early Universe". K.S. has been supported in part by the London Centre for Terauniverse Studies (LCTS), using funding from the European Research Council via the Advanced Investigator Grant 267352.

[1] I. Hinchliffe, F. Paige, M. Shapiro, J. Soderqvist, and W. Yao, Phys.Rev. **D55**, 5520 (1997), hep-ph/9610544.
[2] I. Hinchliffe and F. Paige, Phys.Rev. **D60**, 095002 (1999), hep-ph/9812233.
[3] B. Allanach, C. Lester, M. A. Parker, and B. Webber, JHEP **0009**, 004 (2000), hep-ph/0007009.
[4] K. Desch, J. Kalinowski, G. A. Moortgat-Pick, M. Nojiri, and G. Polesello, JHEP **0402**, 035 (2004), hep-ph/0312069.
[5] K. Kawagoe, M. Nojiri, and G. Polesello, Phys.Rev. **D71**, 035008 (2005), hep-ph/0410160.
[6] H.-C. Cheng, J. F. Gunion, Z. Han, G. Marandella, and B. McElrath, JHEP **0712**, 076 (2007), 0707.0030.
[7] H.-C. Cheng, D. Engelhardt, J. F. Gunion, Z. Han, and B. McElrath, Phys.Rev.Lett. **100**, 252001 (2008), 0802.4290.
[8] H.-C. Cheng, J. F. Gunion, Z. Han, and B. McElrath, Phys.Rev. **D80**, 035020 (2009), 0905.1344.
[9] B. Webber, JHEP **0909**, 124 (2009), 0907.5307.
[10] M. M. Nojiri, K. Sakurai, and B. R. Webber, JHEP **1006**, 069 (2010), 1005.2532.
[11] M. Burns, K. Kong, K. T. Matchev, and M. Park, JHEP **0903**, 143 (2009), 0810.5576.
[12] P. Konar, K. Kong, K. T. Matchev, and M. Park, JHEP **1004**, 086 (2010), 0911.4126.
[13] W. S. Cho, K. Choi, Y. G. Kim, and C. B. Park, Phys.Rev.Lett. **100**, 171801 (2008), 0709.0288.
[14] W. S. Cho, K. Choi, Y. G. Kim, and C. B. Park, JHEP **0802**, 035 (2008), 0711.4526.
[15] M. M. Nojiri, Y. Shimizu, S. Okada, and K. Kawagoe, JHEP **0806**, 035 (2008), 0802.2412.
[16] M. M. Nojiri, K. Sakurai, Y. Shimizu, and M. Takeuchi, JHEP **0810**, 100 (2008), 0808.1094.
[17] S.-G. Kim, N. Maekawa, K. I. Nagao, M. M. Nojiri, and K. Sakurai, JHEP **0910**, 005 (2009), 0907.4234.

[18] M. M. Nojiri and K. Sakurai, Phys.Rev. **D82**, 115026 (2010), 1008.1813.
[19] N. Pietsch, J. Reuter, K. Sakurai, and D. Wiesler, JHEP **1207**, 148 (2012), 1206.2146.
[20] A. J. Barr and C. G. Lester, J.Phys. **G37**, 123001 (2010), 1004.2732.
[21] G. F. Giudice and A. Strumia, Nucl.Phys. **B858**, 63 (2012), 1108.6077.
[22] M. Ibe and T. T. Yanagida, Phys.Lett. **B709**, 374 (2012), 1112.2462.
[23] H.-C. Cheng and Z. Han, JHEP **0812**, 063 (2008), 0810.5178.
[24] C. Lester and D. Summers, Phys.Lett. **B463**, 99 (1999), hep-ph/9906349.
[25] G. Arnison et al. (UA1 Collaboration), Phys.Lett. **B129**, 273 (1983).
[26] A. J. Barr, B. Gripaios, and C. G. Lester, JHEP **0802**, 014 (2008), 0711.4008.
[27] P. Konar, K. Kong, K. T. Matchev, and M. Park, Phys.Rev.Lett. **105**, 051802 (2010), 0910.3679.
[28] T. Cohen, E. Kuflik, and K. M. Zurek, JHEP **1011**, 008 (2010), 1003.2204.
[29] L. Harland-Lang, C. Kom, K. Sakurai, and W. Stirling, Eur.Phys.J. **C72**, 1969 (2012), 1110.4320.
[30] L. Harland-Lang, C. Kom, K. Sakurai, and W. Stirling, Phys.Rev.Lett. **108**, 181805 (2012), 1202.0047.
[31] G. Aad et al. (ATLAS Collaboration), JHEP **1302**, 095 (2013), 1211.6956.
[32] T. Hahn, S. Heinemeyer, W. Hollik, H. Rzehak, and G. Weiglein, Nucl.Phys.Proc.Suppl. **205-206**, 152 (2010), 1007.0956.
[33] W. Beenakker, R. Hopker, and M. Spira (1996), hep-ph/9611232.
[34] M. Cacciari, M. Czakon, M. Mangano, A. Mitov, and P. Nason, Phys.Lett. **B710**, 612 (2012), 1111.5869.
[35] J. M. Campbell, R. K. Ellis, and C. Williams, JHEP **1107**, 018 (2011), 1105.0020.
[36] J. Beringer et al. (Particle Data Group), Phys.Rev. **D86**, 010001 (2012).
[37] J. Alwall, M. Herquet, F. Maltoni, O. Mattelaer, and T. Stelzer, JHEP **1106**, 128 (2011), 1106.0522.
[38] T. Sjostrand, S. Mrenna, and P. Z. Skands, JHEP **0605**, 026 (2006), hep-ph/0603175.
[39] J. de Favereau, C. Delaere, P. Demin, A. Giammanco, V. Lemaître, et al. (2013), 1307.6346.